Fast-charging effects on ageing for energy-optimized automotive $LiNi_{1/3}Mn_{1/3}Co_{1/3}O_2$/graphite prismatic lithium-ion cells

Abdilbari Shifa Mussa[a,*], Anti Liivat[b], Fernanda Marzano[b,c], Matilda Klett[a,c], Bertrand Philippe[d], Carl Tengstedt[c], Göran Lindbergh[a], Kristina Edström[b], Rakel Wreland Lindström[a], Pontus Svens[a,c]

[a] Applied Electrochemistry, KTH Royal Institute of Technology, SE-100 44, Stockholm, Sweden
[b] Department of Chemistry, Ångström Laboratory, Uppsala University, Box 538, SE-751 21, Uppsala, Sweden
[c] Scania CV AB, SE-151 87, Södertälje, Sweden
[d] Molecular and Condensed Matter Physics, Department of Physics and Astronomy, Uppsala University, Box 516, 75120, Uppsala, Sweden

HIGHLIGHTS

- Fast charging increased the rate of ageing.
- The cell capacity fading is dominated by the lithium-inventory loss.
- Gas evolution and lithium plating limit the fast charging capability.
- NMC particle cracking observed after long-time cycling at lower charging rates.
- Ageing is non-uniform in the cell.

GRAPHICAL ABSTRACT
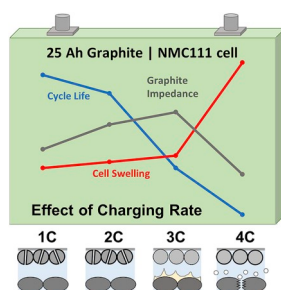
ABSTRACT

The reactions in energy-optimized 25 Ah prismatic NMC/graphite lithium-ion cell, as a function of fast charging (1C−4C), are more complex than earlier described. There are no clear charging rate dependent trends but rather different mechanisms dominating at the different charging rates. Ageing processes are faster at 3 and 4C charging. Cycling with 3C-charging results in accelerated lithium plating but the 4C-charging results in extensive gas evolution that contribute significantly to the large cell impedance rise. Graphite exfoliation and accelerated lithium inventory loss point to the graphite electrode as the source of the gas evolution. The results are based on careful post-mortem analyses of electrodes using: scanning electron microscopy (SEM), X-ray photoelectron spectroscopy (XPS), X-ray diffraction (XRD), and electrochemical impedance spectroscopy (EIS). SEM results show particle cracking independent of the charging rate used for the cycling. XPS and EIS generally indicate thicker surface film and larger impedance, respectively, towards the edge of the jellyrolls. For the intended application of a battery electric inner-city bus using this type of cell, charging rates of 3C and above are not feasible, considering battery lifetime. However, charging rates of 2C and below are too slow from the point of view of practical charging time.

1. Introduction

The electric vehicle (EV) market has significantly increased in volume during the last decade mainly due to the development of lithium-ion batteries with higher energy density, lower price, and longer service life. However, there are still battery-related challenges to

---

overcome before plug-in hybrid vehicles (PHEV) and battery electric vehicles (BEV) can become major players in the vehicle market, especially in the heavy-duty vehicle segment. One such important challenge is driving time versus charging time. A high driving time/charging time ratio may not be a requirement for a passenger car BEV since the majority of the daily trips are short and could be covered by charging during the night [1,2]. In contrast, commercial heavy-duty BEVs typically have an order of magnitude longer daily operating time compared to passenger cars and therefore a high driving time/charging time ratio can be necessary for economic viability. Charging of, for example, BEV buses is only possible during short standstills, or during parking at night which often is less than 5 h. For the latter case, a large battery in the region of 250 kWh or more is required. However, balancing battery size and utilization, a recent study shows that BEV buses with smaller batteries installed and charged at the end stops of the route have the potential to be more cost efficient compared to overnight charged BEV buses when the charging infrastructure is included in the calculation [3]. In this case, the fast-charging capability is more crucial for heavy-duty commercial vehicles than for passenger cars. In combination with energy optimized lithium-ion batteries, fast charging presents an important challenge regarding battery lifetime.

The effects of fast charging on lithium-ion battery ageing has been reported earlier [4–6]. Prezas et al. [4] reported rapid ageing with fast charging on high power 18650 NMC/Graphite cells. Yang et al. [5] cycled high power automotive battery cells at a very high rate (20C) and compared it against reference cycling at 1C rate, and found a negligible effect of the very fast charging on battery ageing. The above studies are performed on power optimized cells which are not primarily applicable for heavy-duty BEV or PHEV. On the other hand, Shirk et al. [6] quantified the ageing effects of fast charging on Nissan Leaf BEV battery packs (LMO-LNO/Graphite) by comparing the capacity fade of a battery charged with DC fast charging (DCFC, ~1.8C) with a battery charged through the on-board AC/DC converter at slow rate level 2 charging (AC L2, ~0.12C). After 80 000 km (50 000 miles) of driving (22–25% total battery capacity loss), the DCFC batteries showed 3% higher capacity loss compared to that of the AC L2. In another study, Tanim et al. [7] compared the ageing of battery packs with the ageing of the corresponding single cells when cycled in laboratory using a simulated Nissan Leaf drive cycle [6] and reported that the difference in capacity fade between the DCFC and AC L2 charging is much lower at cell level compared to pack level. While the studies by Shirk et al. and Tanim et al. are outstanding in their realistic approach, the study is limited to one DC fast charging rate and detailed material analysis has not been reported. In the present study, the effects of fast charging on ageing of energy-optimized lithium-ion cells is investigated with detailed analyses.

Using energy optimized lithium-ion cells in heavy-duty PHEV or BEV applications brings about the trilemma of energy density, fast charging capability, and cycle life. Increasing the energy density decreases the fast charging capability and cycle life [8,9]. The high current and temperature associated with fast charging may decrease battery life significantly [10]. Furthermore, besides changing the chemistry of the electrodes, the high energy density is primarily achieved by optimally increasing its mass loading: increasing the thickness and decreasing the porosity of the electrode. Increase in the mass loading limits electrolyte transport and can lead to lithium plating at the graphite anode surface even at moderate charging rates [8,11]. The resistance of the electrode also increases with the mass loading [9,12] which subsequently increase the battery temperature during operation. Increase in the temperature can worsen other side-reactions such as SEI growth, binder decomposition, electrolyte oxidation, and transition metal dissolution [4,10,13,14]. Furthermore, fast charging increases the susceptibility of electrode particles to crack during lithiation and delithiation due to higher diffusion-induced stresses [15].

In this study, the effects of fast charging (1C − 4C) on the capacity fade and impedance rise of large-format energy-optimized NMC(111)/

graphite prismatic cells are studied. The capacity fade and impedance rise of the cells are periodically measured during the cycling. A non-destructive mathematical cell discharge curve fitting and post-mortem analyses of physical characterization, scanning electron microscope (SEM), x-ray diffraction (XRD), x-ray photoelectron spectroscopy (XPS), electrochemical impedance spectroscopy (EIS), and electrode capacity measurements are performed to study the ageing in detail. Electrode samples at different locations of the jellyroll are analyzed to study non-uniform ageing.

2. Experimental

2.1. Cycling

Commercial prismatic NMC(111)/graphite cells with a rated initial capacity of 25 Ah were acquired from a well-known manufacturer for this study. The dimensions of the cells were 148 × 26.5 × 91 mm (W x D x H), which is the PHEV2 VDA standard (Verband der Automobilindustrie) for prismatic battery cells. Eight cells in total were tested (numbered 1–8), two for each cycling profile.

Cycling was performed between 20% and 80% SOC at different constant current charging rates: 1, 2, 3, and 4C corresponding to 25, 50, 75, and 100 A, respectively. The cells were discharged at constant current of 1C (25 A) in all cases. The SOC window is based on Coulomb counting referring to the latest low-rate capacity measurement part of a reference performance test (RPT) sequence that was performed periodically. There were no rest times between charge and discharge during cycling. The RPTs consisted of a C/4 discharge capacity measurement between 3 and 4.15 V, and direct current internal resistance (DCIR) at 50% SOC consisting of a 50 A charge pulse for 18 s followed by a 50 A discharge pulse for 18 s applied to the cell at rest (1 h). The ohmic resistance was taken as the ratio between voltage drop and applied current after 2 ms of applying the charge pulse, in the following referred to as the 2 ms DCIR. All cycling was done on a PEC SBT0550 equipment from PEC Products N.V. Cycling and reference performance tests were performed at a constant temperature in climate chambers set to 34 ± 1 °C. The chambers were either PU-1KPH from Espec corp. or FD-23 from Binder GmbH. Cell temperatures were monitored using thermocouples type-K attached to a position close to the negative tab on the cells. The thermocouples were insulated from the surrounding air in the climate chamber during testing to ensure sole measurement of the tab temperature. The tab itself is insulated from the cell can in this cell design. The cycled cells were compared with reference calendar aged cells that were stored for 18 months at 25 °C and 3.47 V floating potential.

2.2. Post-mortem analysis

From the batch of 8 cells, one cell from each charging condition (cell numbers 2, 3, 5, and 7) were opened for physical and electrochemical characterization. The opening of each cell was performed in an argon-filled glovebox (H_2O and O_2 < 1 ppm) subsequently after it had reached the end of life. The post-mortem analyses were made within a month time after the opening in order not to alter the electrodes during storage in the glovebox before the analysis. Samples were harvested for the analysis only from the flat regions of the unrolled jellyroll between 30 and 350 cm inward along its length. The spots at which the samples were harvested are named according to the sketch shown in Fig. 1 by mentioning the location along the length first and location along the height next (For example, core-middle means that the sample was taken at core location along the jellyroll length and at the middle along the jellyroll height).

Physical characterization: 40–60 cm^2-size samples containing ~1 g of coating were cut from the Halfway part of the jellyroll choosing the visually uniform regions around the middle spot (Fig. 1). The samples were handled in an inert atmosphere and were not washed. The mass

Fig. 1. Nomenclature of spots tested in the jellyroll.

loading of the electrodes was calculated from the weight measured with a Mettler balance (± 0.2 mg). The thickness was measured at several points in a smaller region of the samples using a Mitutoyo micrometer (± 1 μm).

Brunauer-Emmet-Teller (BET) surface area: Micromeritics ASAP 2020 instrument was used for nitrogen physisorption-based surface area measurements [16] of the same electrode samples used for the physical characterization. The BET analysis were done at 35 °C after 12 h degassing.

XRD: Smaller (3.14 cm^2) samples were analyzed from the halfway-middle region of the jellyroll. Powder XRD was collected under air exposure (~1 h) in CuKα radiation in reflection mode using Bruker D8 instrument equipped with LynxEye detector. Cell parameters for the layered hexagonal $Li_xNi_{1/3}Mn_{1/3}Co_{1/3}O_2$ and graphite models (SG: R-3m) for the positive and negative electrode, respectively were refined using Le Bail method [17] available in Highscore Plus software.

SEM: The SEM samples were prepared in an argon-filled glovebox (O_2 and $H_2O < 1$ ppm) and transferred to the microscope using an evacuated transfer module from Kammrath & Weiss GmbH. The micrographs were collected on a Carl Zeiss Sigma VP scanning electron microscope. The instrument was cleaned by ozone plasma for 60 min prior to all studies to enable high-resolution studies of defoliated structures and Li-metal type morphologies. Generally, the accelerating voltages ranged between 3 and 10 kV and a pressure $< 10e^{-5}$ mBar. An X-Max detector from Oxford, with 50 mm window was used for EDX studies as a verification method, however, XPS was used prior to the SEM studies on several of the samples to get correct elemental composition, including lithium. Moreover, all samples that had been studied by means of XPS were thereafter investigated by SEM. The positions of studies were carefully noted and samples transferred in an inert atmosphere between the SEM and the XPS.

XPS: The XPS measurements were performed on a Perkin Elmer PHI 5500 instrument using monochromatized Al Kα radiation (hν = 1486.6 eV). A pass energy of 23.5 eV was used and the pressure in the analysis chamber was about 10^{-9} Torr. The XPS samples were prepared in the glovebox and transferred to the spectrometer in a sealed vessel to avoid air exposure. The collected electrodes were not washed with any solvent to avoid the dissolution of SEI components. Peak fitting was carried out with CasaXPS, and the energy calibration was done using the hydrocarbon (C−C, CHx) peak at 285 eV as an internal reference for the graphite anode; while the peak originating from the conductive additives (graphitic carbon) was set at 284.5 eV for the NMC cathode. No charge compensation was used in this study. The surface of the NMC cathode facing the separator was investigated. For the anode, as an alumina layer was covering the graphite electrode, XPS was done on the graphite surface facing the current collector after peeling of the composite using a copper tape. Quantification was performed on the basis of Scofield's relative sensitivity factors [18].

Electrochemical characterization: For each of the harvested double coated electrode samples, one side was gently cleaned using N-methyl-2-pyrrolidone (NMP) soaked cotton buds in order to expose the current collector for external electrical connection. Care was taken to avoid contaminating the other side with the NMP. For electrochemical characterization, graphite and NMC electrode samples of 10 and 12 mm diameter, respectively, were cut out from the cleaned regions. The

electrode capacity measurements were performed in half-cell set-up using a lithium foil counter/reference electrode, a Celgard separator (PP/PE/PP, 2320), and a commercial 1 M $LiPF_6$ in 1:1 ethylene carbonate (EC): diethyl carbonate (DEC) electrolyte (Merck LP40). The capacity of graphite was measured between 0.002 and 1.5 V at C/25 rate and between 2.9 and 4.2 V at C/36 rate for the NMC electrode. Duplicate cells were measured in each case. Thereafter, the graphite electrodes were set to 0.12 V vs. Li/Li^+ and the NMC electrodes to 3.95 V vs. Li/Li^+ in the corresponding half-cell before preparing symmetric cells for the EIS measurement. EIS was performed in the frequency range of 100 kHz–5 mHz for the NMC/NMC and 100 kHz–10 mHz for the graphite/graphite configuration by applying 5 mV root-mean-square (rms) sinusoidal perturbation at open circuit voltage condition. The electrochemical measurements were performed at 25 °C using Gamry PCI4/750 or Solatron 1286/1287 potentiostat.

Cell voltage fitting: Cell voltage fitting was performed in order to quantify lithium inventory and active electrode material losses. The method is based on the electrochemical principle that electrode potential is independent of its size and assumes that its equilibrium potential as a function of Li concentration is constant throughout the battery life. Hence, the cell discharge curve ($V_{cell}(Q)$) at any stage of ageing can be reproduced by using the independently measured discharge curves of small electrodes (v(q)), harvested from a fresh cell and measured in half-cells (lithium counter electrode). For the cell discharge curve reproduction, the small electrode capacities (q) are first scaled up by a factor (S) to fit the capacities of the larger electrodes in the reproduced cell. Second, the scaled-up electrode capacities are shifted by (δ) relative to the beginning of cell discharge curve to account for the non-accessed capacities of the electrodes in the reproduced cell depending on the cycling range of the half cells and the capacity loss of the reproduced cell. Considering these, the cell discharge curve reproduction can be achieved by using Equation (1). The detail description of the mathematical formulation and fitting is given in our previous work [19].

$$V_{cell}(Q) = v_{pos}\left(\frac{Q-\delta_{pos}}{S_{pos}}\right) - v_{neg}\left(\frac{Q-\delta_{neg}}{S_{neg}}\right) \tag{1}$$

The parameters on the left-hand and the right-hand sides of Equation (1) are for the reproduced cell and for the half cells, respectively. Note that Q is the discharged capacity of the cell at a certain time t after the beginning of discharging, and not necessarily the full discharge capacity of the cell.

The losses of active cathode material (LACM) and active anode material (LAAM) can thus be calculated from the ratio of the scaling factors (S) obtained from the fitting at the EOL and BOL as shown in Equations (2) and (3), respectively.

$$LACM = \frac{S_{pos,EOL}}{S_{pos,BOL}} \tag{2}$$

$$LAAM = \frac{S_{neg,EOL}}{S_{neg,BOL}} \tag{3}$$

The loss of lithium inventory (LLI) corresponds to the difference in the lithium leaving the negative electrode ($S_{neg}*dq_{neg}/dt$) and the lithium entering into the positive electrode ($S_{pos}*dq_{pos}/dt$) during cell discharge and can be calculated according to Equation (4).

$$\frac{dLLI}{dt} = S_{neg}\frac{dq_{neg}}{dt} - S_{pos}\frac{dq_{pos}}{dt} \tag{4}$$

Integrating Equation (4) and ignoring negligible values gives Equation (5) for the LLI between the BOL and EOL during cycling.

$$LLI \approx (\delta_{neg,EOL} - \delta_{pos,EOL}) - (\delta_{neg,BOL} - \delta_{pos,BOL}) \tag{5}$$

In this work, the C/25 discharge curves of the cells between 3 and 4.2 V was reproduced. A non-cycled prismatic cell representative of the
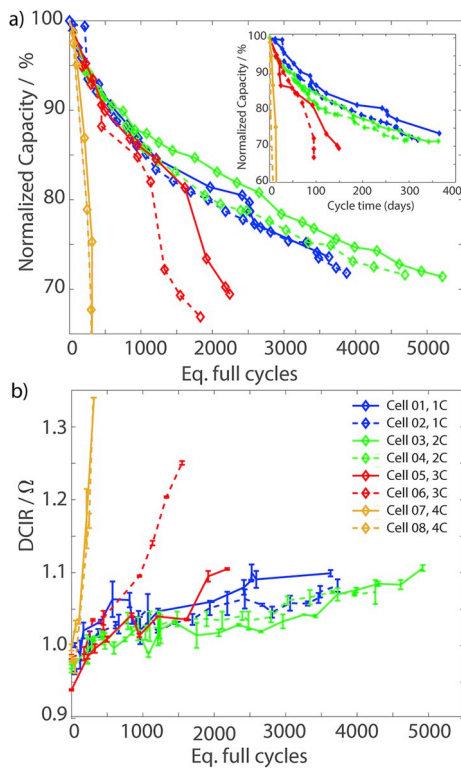
Fig. 2. a) Capacity fade vs. number of equivalent full cycles (inset: capacity fade vs. cycling time). b) 2 ms direct current internal resistance (DCIR) vs. equivalent full cycles at 50% SOC. Error bars represent the spread between charge and discharge.

beginning of life (BOL) condition was opened and 10 mm diameter electrodes were harvested from both the NMC and graphite electrodes to construct the half cells. The NMC/Li and graphite/Li half-cells were cycled at C/25 rate between 2.9 – 4.3 V and 0.002–1.5 V, respectively. A non-linear least square 'Levenberg-Marquardt' algorithm in Matlab 2015a was used for the fitting in Equation (1).

3. Results

3.1. Cycling performance

Fig. 2a shows capacity fade versus current throughput in number of equivalent full cycles (2 × 25 Ah) at different charging rates. It can be seen that the general order of the capacity fade in an increasing order is 2C < 1C < 3C < 4C. The three common phases of capacity fade can be observed in the figure; an initially high rate capacity fade for a certain number of cycles (Phase 1) before the deceleration (Phase 2) is observed for cells cycled at 1C − 3C. This characteristic has been attributed in literature [20] to a high rate of cyclable lithium loss as the solid electrolyte interphase (SEI) grows in phase 1. As the SEI grows thicker, its passivating property decreases the rate of cyclable lithium loss in phase 2. Cells cycled at 3C charging show a third phase of accelerated capacity fade (Phase 3). This behavior has been attributed to lithium plating and an accelerated active material loss [20,21]. The cell cycled at 4C charging rate shows a high rate capacity fade for approximately the first 100 cycles (Phase 1) followed by acceleration from 100 to 300 cycles (Phase 3) before finally reaching sudden death. The sudden death in the 4C cells is due to the activation of the current interrupt device (CID) that irreversibly disconnected the positive tab from the jellyroll. Activation of the CID is specifically caused by extensive internal pressure from gas build-up in the cell although none of the cells vented. At the end of cycling, the 4C cells were swollen to about 40 mm in thickness in comparison to ∼ 32 mm for the other cells

cycled with a charge rate of 1C − 3C. The fresh cell had 27 mm ± 1.5 mm thickness, showing that all cells swell to a certain amount. The faster capacity fade in the 1C charging compared to the 2C when plotted as a function of the equivalent full cycle might be related to the longer calendar time during cycling at the 1C. However, as shown in the inset of Fig. 2a, the difference in the rate of capacity fade between the 1C and 2C cells is not large enough to confirm this.

Fig. 2b shows the corresponding full cell DC-impedance measurements at 50% SOC. It can be seen that the DC impedance rise follows the same order as the capacity fade (2C < 1C < 3C < 4C). This indicates that the impedance data could be used for estimation of capacity fade during usage for this particular cell. Finally, it should be noted that cycling at a higher rate causes a higher heat production and possibly a higher ageing rate. However, in this case, any significant effect of different cell temperatures resulting from our cycling scheme is deemed unlikely and not the root casue of the different aging behavior observed. The cells were kept in a temperature chamber (34 ± 1 °C), and monitoring the tab temperature of the cells at the different C-rates showed no significant difference between them (Supplementary information (SI): Table S1). It should be noted that the tab in this cell design is insulated from the cell can but directly in contact with the current collectors and jellyroll, which provide a better indication of interior temperature than measuring on the cell can. The temperature sensor was also insulated to reduce the impact of chamber temeperature. In addition, previous work on the same cell type only showed a small (< 2.5 °C) difference between tab temperature and the temperature in the centre of the jellyroll [22], supporting our statement that difference in temperature is not the qualifying aging factor for the higher cycling rates compared to the lower. The highest tab temperature of 41.6 °C was measured on the 3C-cycled cell 05, and the second highest tab temperature of 40.6 °C was measured on the 4C-cycled cell 08.

3.2. Physical characteristics of harvested electrodes

One cell of each charging condition (cell no. 02, 03, 05 and 07) was opened for physical and electrochemical characterization. Upon opening, all the graphite electrodes had a light grey appearance (SI: Fig. S1), likely due to a thin alumina coating that was found on the surface of the electrode facing the separator (confirmed by SEM/EDX below), and also from the dried electrolyte. The calendar aged electrode appeared intact and smooth while all the cycled electrodes had a wrinkled appearance (SI: Fig. S1) likely due to electrode swelling in the constrained geometry of the jellyroll in the can. For the 3C graphite electrode, the patterns were also trailed by golden, metallic-appearing, deposits of plated lithium metal. Delamination of the electrode coating from the current collector could also be observed especially for the 4C cell at several locations along the winding. In all cases, the delamination was more prevalent closer towards the jellyroll core. The wrinkled appearance was also mirrored on the cycled positive electrodes, whose overall appearance were more similar to the calendar aged cell and less brittle than the cycled graphite.

Fig. 3 a-c shows changes in mass, thickness, and BET surface area, respectively, after cycling for the positive and negative electrodes. The corresponding absolute values are found in the SI: Table S2. Fig. 3b shows that cycling leads to a significant (8–14%) increase in the negative electrode loading weight. This increase is smaller at higher charging rate, indicating that the time of cycling contributes more to the mass gain than the charging rate. Considering the very fast ageing of the 4C cell, however, the rate of loading increase is significant for this cell. The thickness of the negative electrode increases in the same order of magnitude as the loading. However, the trend in the thickness increase is not clear as the nonuniformity of the electrolyte deposits on the unwashed electrodes causes a large spread in the measurements. Some small changes are observed in the positive electrode but with no visible trend. The 3C and 2C electrodes show increase in the thickness
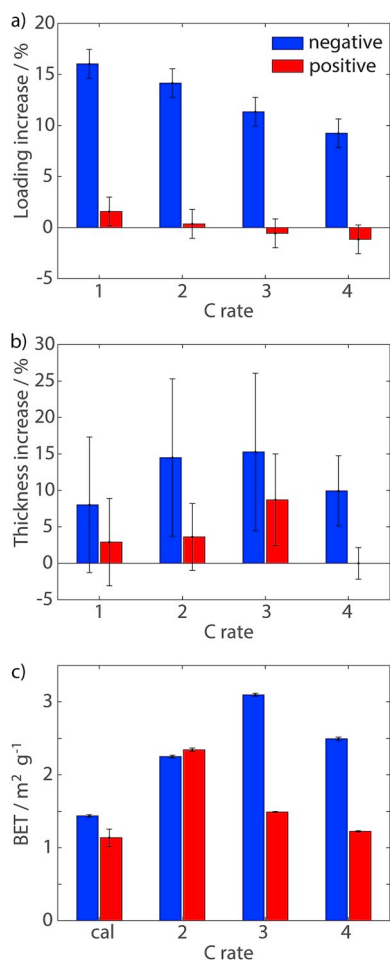
Fig. 3. Physical characterization in terms of changes in the single-sided mass loading (a) thickness (b) for the cycle-aged electrodes relative to the calendar-aged electrodes, and the Brunauer-Emmett-Teller (BET) surface area of the aged electrodes (c).

Fig. 4. SEM images of negative (a–d) and positive (e–h) electrodes. a) Calendar-aged (CAL), showing the Al_2O_3 coating; b) Grain with surface structure found on CAL, 1C and 2C (image from 1C electrode); c) Li-plated surface structure on 3C; d) Defoliated grains in 4C; e) Typical particle agglomerates in CAL, 1 and 2C (image from 1C electrode); f) Cracked particles found in 1C, 2C, and 3C; g) Bare particles in 3C, and h) Covered particle without cracks in CAL and 4C (image from 4C electrode).

and BET surface area, respectively, while other properties remained more or less unchanged within the measurement uncertainty. Due to the very brittle electrode of the 1C cycled cell, it was not possible to make the BET measurement on this sample.

3.3. Surface analysis of aged electrodes

Fig. 4 shows some selected SEM images typical for the positive and negative harvested electrodes. As seen in the lower left corner of Fig. 4a, showing a cross-section of the calendar-aged sample, the graphite electrodes were coated by a thin layer of alumina particles facing the separator. The images of the negative electrode were hence taken from the surface facing the copper foil after it had been peeled off from the metal foil. The typical graphite flakes of up to 20 μm are visible in Fig. 4 (b, d). The flakes are covered by a finely textured layer, covering the majority of the particles in CAL, 1C, and 2C samples shown in Fig. 4b. For the 3C and 4C samples, this texture was absent in some areas (Fig. 4d). As mentioned previously, the 3C graphite electrode appeared to be covered by a shiny metallic layer, predominately in areas close to the edges. Fig. 4c displays an image from these regions showing a similar net-like pattern appearance to Li-plated graphite electrode material [23] and Li-metal in Li-sulfur batteries [24], i.e. with pit corroded parts and filament (dendrite) growth. This pattern was observed only on the 3C sample but it is likely that plating also occurs during 4C charging, but because of the rapid sudden death of the 4C cell, an irreversible film was never able to form. Completely exfoliated
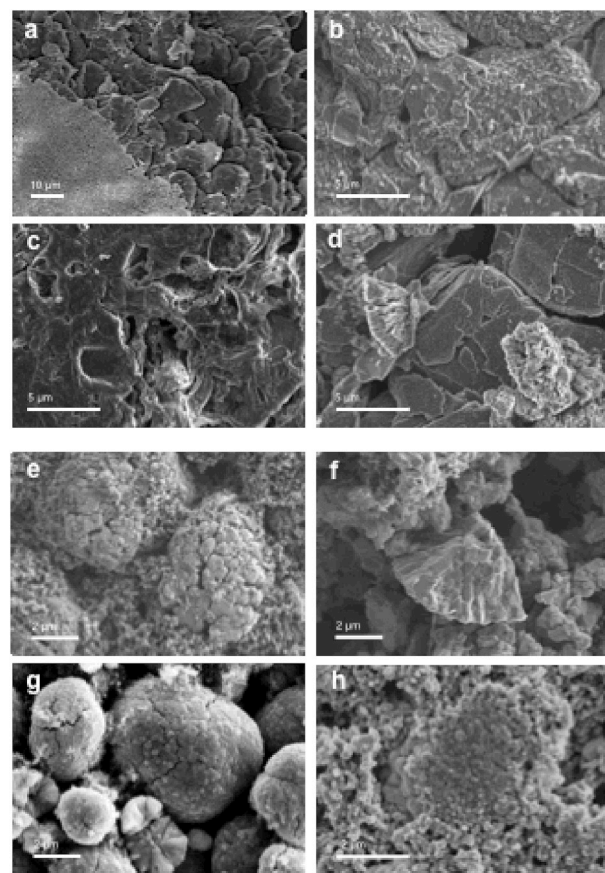
graphite particles were only observed at the 4C cycled sample (Fig. 4d). The two specific ageing patterns for 3C and 4C are in accordance with the observed increase in the surface area.

The positive NMC electrode is typically composed of rounded secondary particles up to 5 μm in diameter as displayed in Fig. 4e. At the surface, the grains are covered and embedded in a matrix of smaller particles of around 300 nm in diameter presumably consisting of conductive carbon. The secondary particles are intact on the calendar-aged electrodes, while cracks can be observed in the cycled electrodes. On the 1C and 2C samples, some grains seem so fragile that they have become completely pulverized in the SEM sample, displayed in Fig. 4f. Significant particle fracturing was also observed in the 3C sample. Overall, the 1C and 2C charged positive electrodes were more severely damaged and the 3C stands out with its bare appearance in absence of the smaller particles, while 4C is obviously less affected.

3.4. X-ray photoelectron spectroscopy (XPS)

3.4.1. Graphite anode and SEI

The organic part of the SEI can be investigated from the analysis of the C1s and O1s spectra displayed in Fig. 5a for the halfway-middle position. The spectra for the other positions can be found in SI: Fig. S2. The spectra are consistent with the expected profile for aged (either calendar or cycling) graphite electrodes, consisting predominately of the degradation products of the electrolyte solvents covering the graphite material [25].
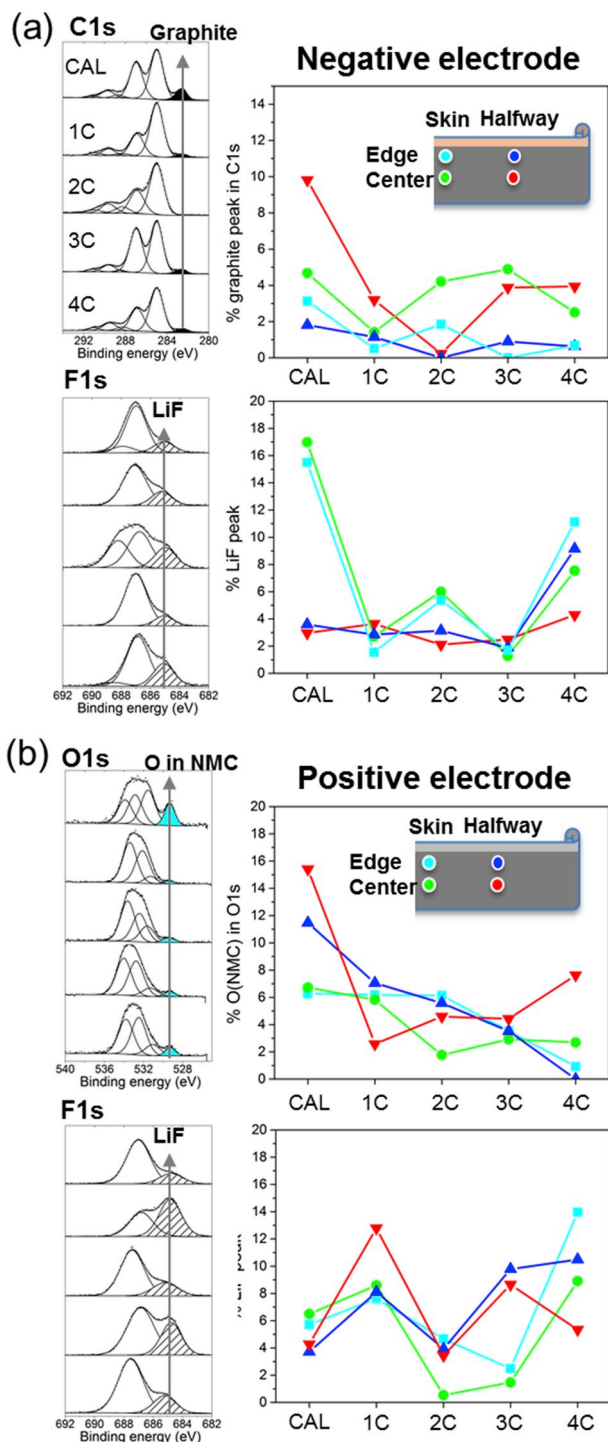
Fig. 5. XPS data from harvested negative electrodes, C1s and F1s (a) and positive electrodes, O1s and F1s (b) from the calendar, 1C, 2C, 3C and 4C cells. The spectra from halfway-centre (red point) are displayed to the left and the evolutions of the proportion of the indicated peak to the full spectrum are shown in the graph to the right. Spectra from the other points are found in the SI. (For interpretation of the references to colour in this figure legend, the reader is referred to the Web version of this article.)

For C1s, no significant trends can be observed with increasing charging rate. The contribution of the graphite peak at low binding energy (∼283 eV) can be used here to estimate the relative coverage of the graphite grain by the SEI. The larger contribution of this peak to the C1s spectra, the thinner is the SEI layer. The relative percentage of graphite detected (Fig. 5a, values are also given in Table S3) show that

the SEI is thicker on the edge than toward the centre of the electrode independently of the ageing conditions. For the SEI thickness, no clear trends with cycling rate is observed except that the SEI is generally thinner in the calendar aged than in the cycled negative electrodes.

Similarly to C1s, no trends could clearly be observed with increasing charging C-rate for the corresponding O1s core level spectra (SI: Fig. S3). The presence of Li_2O (O1s peak at 528 eV) is only observed in the centre part of the jellyroll in a proportion that correlates well with the amount of graphite observed in C1s spectra (Fig. 5a). Li_2O cannot be detected at the edge of the electrode corresponding to the spot where the SEI is thicker. This similar behavior is consistent with the presence of Li_2O near the graphite surface [23].

The inorganic part of the SEI, mainly consisting of deposited salt and its degradation products can be studied via the F1s and P2p core level spectra in Fig. 5a and SI: Figs. S2 and S4. The P2p consists mainly of two components: a $LiPF_6$ contribution from remaining salt and (fluoro) phosphates. The amount of phosphor is quite homogeneous in the SEI (∼4–6%) and do not show any dependence on the charging rate or the position. From the F1s spectra (Fig. 5a), the peak at about 687 eV assigned to $LiPF_6$ salt dominates but LiF is also detected at 685 eV (hatched peak). The proportion of LiF appears to be higher in all the spots for the highest charge-rate sample (4C). Interestingly, it is also higher for the calendar aged samples in the skin part of the jellyroll, but not in the halfway part. Since the LiF concentration is similar at the edge and in the centre of the electrode, we can conclude that salt degradation on cycling does not differ in the position of the jellyroll on the negative electrode.

Note that the samples were unwashed and that the peeling-off of the composite from the current collector could damage the SEI, leading to the exposure of graphite surface in some spots. The uneven drying of the electrolyte together with the SEI removal can also explain the absence of clear and neat trends in the correlation between the SEI thickness, composition and charging rate.

An attempt was also made to investigate the Li1s in order to prove the existence of metallic Li on the 3C sample. However, the surface is found to be covered by LiF and Li_2CO_3 (Figs. S5 and SI), probably formed by reaction with the electrolyte or during storage in the glovebox after the cell disassembly. Considering the surface sensitivity of the technique, it is, therefore, hard to say from this analysis if a Li metal film is formed under the surface layer.

3.4.2. NMC cathode and SPI

The O1s and F1s spectra from the positive electrode are presented in Fig. 5b and in SI: Fig. S6.

An estimation of the NMC coverage by the solid permeable interphase (SPI) can be made from the transition metal oxide peak (blue peak in Fig. 5b): in the O1s spectra. The larger the relative area of the peak, the thinner the SPI. The graph in Fig. 5b shows the proportion of this blue peak compared to the total area of the O1s spectra (values can be found in SI: Table S3). The SPI is thinner on the calendar aged cell and is generally getting thicker at increasing charge rate, especially at the edge of the jellyroll. At the centre, however, the SPI thickness does not show such clear trend.

The F1s and P2p (SI: Fig. S4) spectra provide information about the inorganic part of the SPI. The total amount of phosphorus is generally lower in the SPI (0.5–3%) compared to the SEI but appear in both cases to be higher at the 4C samples on the edge of the jellyroll. However, the proportion of LiF in SPI is higher for the longest lasting cycle-aging (1C).

3.5. X-ray diffraction

The XRD patterns of the negative electrodes displayed in Fig. 6 show that the surface is covered with alumina, with narrow peaks implying much larger particles than that of nano-size coatings. Sharp peaks associated with Li_2CO_3 are present on the 3C and 4C samples and to some
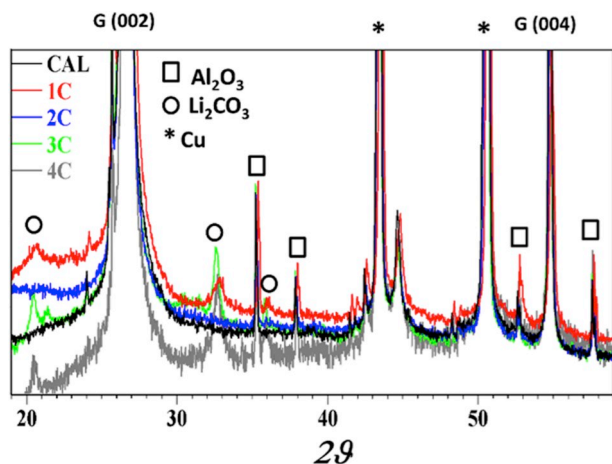
Fig. 6. XRD patterns of the aged negative electrodes magnified to show the small intensity reflections of impurities (marked). The intense reflections of graphite also marked.

extent on the 1C sample. However, no Li_2CO_3 was found on the 2C and calendar-aged electrodes. The presence of Li_2CO_3 only on the 1C, 3C, and 4C samples may imply that the carbonate deposits vary substantially across the surface of the electrodes, since no clear trend was seen for these species in XPS data either.

3.6. Electrochemical characterization

A typical cell voltage fitting for the estimation of lithium inventory and active material losses is shown in Fig. 7a. Good fitting with an average error of $\sim 3\,mV$ between the experimental and calculated cell voltage curves is obtained for the cells cycled with $1C - 3C$ charging rate. It can be seen that the high SOC region of the graphite is less accessed at the EOL, shifting the point of maximum graphite lithiation to the right relative to that at the BOL. Fitting of the 4C cell was not performed because the shape of the discharge curve was changed too

much at the EOL that the fitting error became unacceptable. However, shifting of its electrode potential window was observed experimentally for the 4C cell (cell 08) during the last 147 equivalent full cycles as shown in the SI: Fig. S7. During this time, the 4C cell is continuously discharged to successively lower cell voltage, due to cyclable lithium loss when cycling the cell in a fixed capacity window, while keeping the upper cell voltage relatively unaffected indicating that the graphite electrode potential is shifted and its higher potential region is progressively more accessed. When the remaining capacity is recalculated during a periodical reference measurement, cycling should return to the desired SOC-window.

Fig. 7b shows results of the estimated losses in lithium inventory and active electrode material and the measured cell capacity loss. The loss of lithium inventory is very close to the total cell capacity loss, indicating that it is the dominating mode of ageing for the cells cycled at $1C - 3C$ charging rate. Significant active material losses are revealed from both the calculated (Fig. 7b) and the measured values (Fig. 7 c-d). However, these do not contribute significantly to the cell capacity losses due to the presence of excess active material both at the beginning and end of discharge at the EOL (shown as an example in Fig. 7a for the 1C cell). Note that no capacity loss is observed for the positive electrode harvested from the 4C cell, in line with the pristine appearance in SEM and minor changes in physical data of that electrode. The capacity loss of the corresponding negative electrode is, however, significant and likely associated with the defoliation of the graphite observed by SEM.

The NMC active material losses calculated from the voltage fitting are larger than those experimentally determined from the harvested electrode samples (Fig. 7 b-c). This can be explained by the fact that the samples were taken from flat areas showing lower contact losses due to delamination than the curved part of the jellyrolls as observed in a previous study [26]. In addition, material losses induced by trapped gas that prevent access to part of the available electrode material [27] before the cell opening are not captured in the post mortem analysis. However, the measured active mass loss in the harvested graphite electrode samples is slightly larger than that calculated from voltage fitting of the prismatic cells. This is probably a consequence of unavoidable active material loss introduced during sample cutting as these
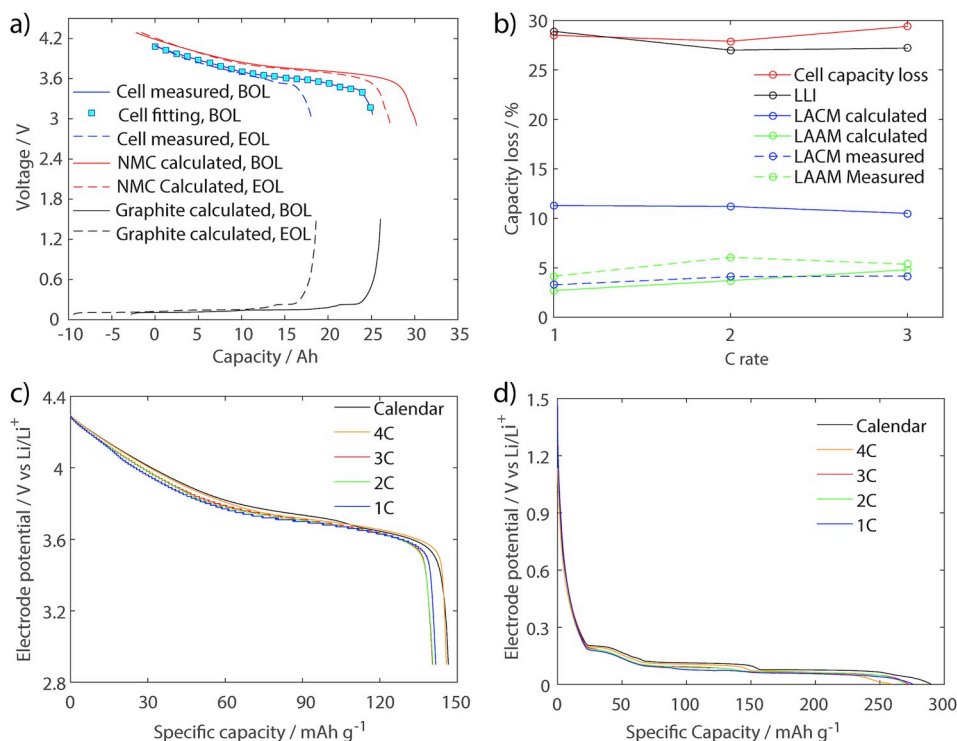

Fig. 7. Calculated and measured capacity loss data of the cells cycled at different charging rates: a) Example of curve fitting for the 1C cell. b) Measured cell capacity loss and calculated losses of lithium inventory (LLI), cathode material (LACM), and active anode material (LAAM). c) Specific capacity of the harvested NMC electrodes. d) Specific capacity of the harvested graphite electrodes.
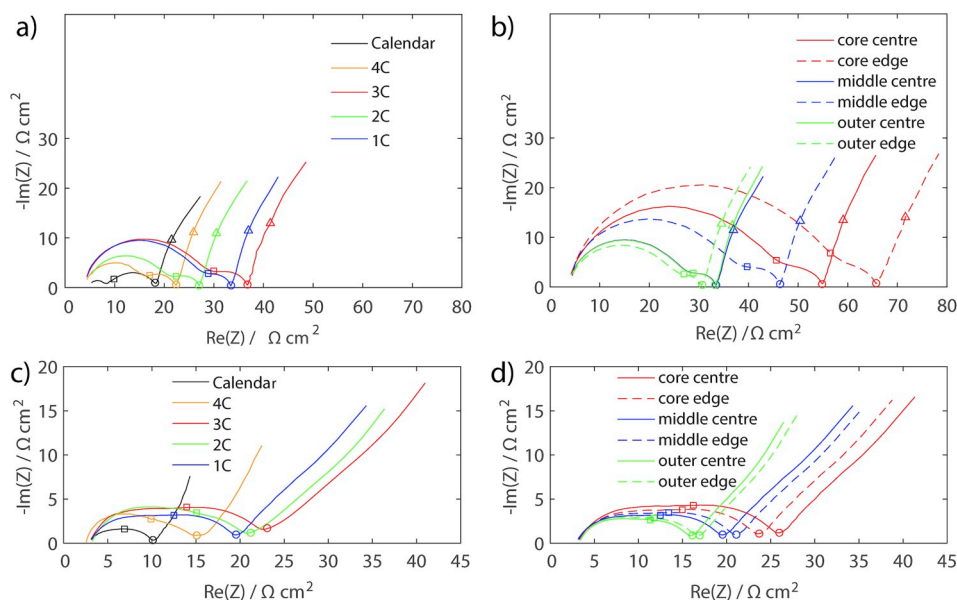
Fig. 8. Impedance spectra for symmetric cells harvested from the different locations of the calendar aged and the cycled cell jellyrolls: a) NMC from the middle centre location. b)NMC from the 1C cell. c) Graphite from the middle centre location. d) Graphite from the 1C cell. (Notations: c-d) □ 251 Hz, o 0.795 Hz, and Δ 0.01 Hz. c-d) □ 1000 Hz and o 5 Hz).

samples were very brittle.

The impedances in Nyquist plot of symmetric cells constructed from the harvested electrodes of the calendar aged and cycled cells are shown in Fig. 8(a–d). Both the electrode impedances are increased after cycling (Fig. 8 a,c). The impedance rise of the NMC is generally larger compared to the graphite. The general trend in impedance rise with charging rate (4C < 2C < 1C < 3C, Fig. 8 a) follows that of the full cell (2C < 1C < 3C < 4C, Fig. 2), with the one clear exception that the 4C electrode impedence is the lowest while that of the 4C full cell is the highest. For the graphite (Fig. 8c), the 1C and 2C spectra are quite similar and placed in between 3C and 4C in terms of impedance increase. It can be seen that, for both NMC and graphite, the 3C cycled electrodes are the most degraded while that of the 4C is the least, in agreement with the other post-mortem material analyses. The substantial ageing of the electrodes from the 3C cell compared to that of the 4C cell is due to the higher capacity through-put in the 3C cell during cycle ageing. The reason for the higher full cell impedance for the 4C cell is claimed to be related to cell swelling being a consequence of gas evolution in the cell (SI: Fig. S8). Gas bubbles trapped between the electrodes in the jellyroll can cause local voids that physically separate the positive and negative electrodes and remove the electrolyte from the separator disrupting the ionic conduction [27], leading to an increase in cell impedance.

In Fig. 8, the most notable increase in impedance of the NMC is in the width of the first depressed semi-circle at high frequency, which is usually attributed to an increase in the surface film ionic-migration resistance or to contact resistance between the electrode particles, the conductive additive and the current collector [26,28–31]. The diameter of the overlapping semi-circles in the graphite electrode increases with ageing presumably related to an increase of SEI thickness that affects the charge transfer resistance seen at intermediate frequencies. The length of the Warburg tail at low frequency increases in both cycled NMC and the graphite electrodes, showing an increase in the diffusion resistance. Furthermore, the EIS data confirm that the cycle ageing is non-uniform along the length and height of the jellyroll. Fig. 8 b and d show the impedance spectra at different locations for the NMC and graphite electrodes, respectively, harvested from the 1C cycled cell. Generally, there is a higher impedance towards the edge along the height direction, and towards the core in the lengthwise direction of the jellyroll. This inhomogeneous ageing is likely induced by nonuniform distribution of pressure, temperature, and current in the large format prismatic cell [32].

4. Discussion

In this study, we have investigated the fast-charging capabilities of energy-optimized cells looking at changes in cell performance during cycling and analyzed the physical, chemical, and electrochemical changes of the electrodes to further deepen the understanding of the failure mechanisms. The results clearly show that fast charging above 2C rate significantly accelerates battery ageing but with different ageing mechanisms dominating at the different rates investigated.

The results show that the 4C cell experience fast ageing and eventually a sudden death after about 300 charge-discharge cycles. The post-mortem material characterizations reveal that the NMC material is not significantly affected by the cycling. The graphite electrode shows a small increase in mass, thickness, and active area, and loss in the capacity that can be associated with the significant defoliation observed by the SEM. However, the minimal amount of deposits or texture on the graphite flakes and very small changes in EIS, indicate that the SEI growth has been limited. This electrode also contains Li_2CO_3 and LiF, more stable inorganic SEI degradation products which are conversions from metastable organic components like lithium alkyl carbonates at an elevated temperature [10]. The 4C cell shows the largest impedance rise even though the corresponding harvested electrodes have the lowest. This is most likely due to gas evolution in the cell inducing physical separation of the electrodes and obstructing the ionic transport as a result. The gas evolution is deduced from the activation of the CID and the significant swelling of the cell that could not be explained only by the corresponding increase in electrode thickness. Gas evolution can arise from electrolyte oxidation at the positive electrode or reduction at the negative electrode. The electrolyte oxidation is predominantly due to activation of the sacrificial shut-down additives if present in the electrolyte. In a cyclic voltammetry test performed with harvested electrolyte from a fresh cell, oxidation peaks were first registered at 4.5 V vs. Li/Li^+. In this study, however, the cell voltage was never allowed to exceed 4.1 V during cycling. Further, the cell voltage fitting analysis (Fig. 7) indicates that the positive electrode potential on average is limited to approximately 4.2 V. Certain inhomogeneity and local hotspots due to cell size and geometry can be expected in the large cells, as also shown in this study with the variation in electrochemical and material properties at different locations in the cell, but overpotentials of more than 0.3 V cannot be supported. Furthermore, no significant sign of oxidation products from the shut-down additives could be revealed from the post-mortem analysis of the NMC electrode (Fig. 8a). If the gas evolution were due to oxidation of the additives at

the positive electrode, it would result in a significantly larger increase in the charge transfer resistance [33] than observed in Fig. 8a. Hence, the extensive gas evolution is argued to be initiated by reduction reactions on the negative electrode. Reduction of protonated compounds formed at the positive electrodes has been reported to form gas, e.g. hydrogen, at the negative electrode [34]. The extensive graphite exfoliation that was observed (SEM) is also indicative of gas evolution in the graphite electrode [10]. Gas evolution has been previously observed [27,35] to be accompanied by accelerated loss of cyclable lithium presumably to the formation and growth of the SEI layer. The cell cycled at 4C in our case showed a capacity loss of 21% (C/4) in less than 300 cycles, as compared to about 27% loss (mainly due to lithium inventory) in about 2000, 3750, and 4750 equivalent full cycles for the 3C, 2C, and 1C cells, respectively. Even though not calculated, the cyclable lithium loss in the 4C cell is experimentally observed from the cell voltage shifts during cycling (SI: Fig. S7). The delithiation of the graphite electrode can take place at a higher potential at the end of discharging if the losses of cyclable lithium is large. This can induce breakdown of the SEI and result in gas generation, as was reported by Michalak et al. [35].

The 3C cells experienced a longer period of cycling compared to the 4C cells and the corresponding harvested electrodes of the opened cell are the most aged. The third capacity fading phase observed for the 3C cells (Fig. 2a) has been linked in literature to lithium plating that leads to a non-linearly accelerated capacity fade [36]. Visually extensive gold-like deposits of plated lithium were only observed for this cell. The reason that lithium plating is observed in the 3C rather than the 4C cell is likely due to the higher number of cycles the 3C cell was subjected to. The slower kinetics in the graphite electrode for the 3C cell seen in the electrode impedance measurements could increase the probability of plating. Even though the graphite grains are not covered by the fine texture as observed for 1 and 2C, large areas are significantly altered on the electrode in which a continuous layer growth and dissolution have taken place, forming the net-like morphology typically observed for Li-plating [23]. The NMC electrode was degraded with losses in conductive carbon particles and secondary particle cracking, which can cause a decrease in the electronic conductivity and contribute to the large increase in the high-frequency semi-circle impedance shown in Fig. 8a.

The cell cycled at 1C charging rate show faster capacity fade than the 2C cell. The appearance of the 1C electrodes is very similar to the 2C electrodes, with cracks on the positive electrode and a texture on the graphite flakes. However, the 1C charge rate results in a larger high-frequency semi-circle of the positive electrode, probably indicating more contact loss, especially at the edge location of the jellyroll. Furthermore, the graphite impedance is higher, pointing towards more SEI formation. The reason for the faster ageing rate for 1C in comparison to 2C might be due to the longer calendar time of the later during cycling but this is not clear from the results.

The cells age non-uniformly along the width and length of the jellyroll. More ageing is observed towards the edge along the width direction and towards the core along the length direction (Fig. 8 b,d). Non-uniform distribution of temperature, pressure, and current could cause the non-uniform ageing. However, the non-uniformity shown by the EIS along the length of the jellyroll did not show a clear trend in the XPS. This could be due to some mechanisms, for instance contact resistance, that can not be captured by the XPS. In a parallel study [26] on the 1C NMC electrode, the increased size of the high-frequency semi-circle was shown to be associated mainly to the contact resistance between the current collector and the active electrode coating, even though other things such the surface film resistance to ionic migration also contributes. Hence, this point towards the increasing trend in impedance towards the core of the jellyroll is mainly due to the contact resistance between the current collector and the active electrode coating, and may not be due to a difference in the surface film properties. Increasing current collector delimitation from the active

electrode coating towards the core of the jellyroll was also observed visually during the cell opening as described in section 3.2.

From an application point of view, charging at a 3C-rate between 20% and 80% SOC would require 12 min battery charging time in a BEV bus. This would probably be acceptable for a bus occasionally charged at the end stops, even if shorter charging time would be preferable. At a 2C-rate the charging time would be 18 min, which may be too long for this type of application. A charging frequency of about 800 equivalent full cycles per year is realistic for an inner city BEV bus that is fast charging every 70 km [37]. When comparing those numbers with our results it is obvious that a 3C-rate charging is not feasible for this type of battery cell, even in a restricted SOC-window since it would require a battery exchange in about every second year. However, 2C-rate charging could be feasible since the battery, in that case, has the possibility to last for 6 years with a capacity retention of 70% or more. To be able to reduce charging time using this cell type in a fast charge BEV bus application, it would be necessary to restrict cycling to an even smaller SOC-window to obtain sufficient lifetime. This would, of course, require increasing the total capacity of the battery system to meet the desired driving range between charging opportunities and a lowered degree of battery utilization. The decreased effective energy density of such a NMC(111) based BEV bus battery suggests that other more suitable battery cell chemistries could be considered, for example batteries based on lithium iron phosphate or lithium titanate.

5. Conclusion

In this work, the effects of fast charging (1–4C in 20–80% state-of-charge range) on the ageing of a 25 Ah energy-optimized automotive prismatic lithium-ion cell based on NMC/graphite chemistry is investigated by post-mortem physical, chemical, and electrochemical characterizations, and cell voltage fitting analysis.

The results show that cycling at 3C and 4C charging rates cause accelerated cell capacity fade and impedance rise. The post-mortem analysis of the electrodes' physical properties, XPS, XRD, and SEM show no clear trends with the charging rate but rather different mechanisms dominating at the different charging rates. The cycling at 3C charging rate results in lithium plating, which was not observed for the other charging rates including 4C, indicating that lithium plating arises at fast charging after a longer period of cycling. The 4C charging causes extensive gas evolution as was implied from the activation of the current interrupt device and the significant cell swelling that was not associated with a thickness increases of the corresponding electrodes. The exfoliation, presence of more lithium fluoride (LiF), and accelerated cyclable lithium loss points to the graphite electrode as the source of the gas evolution. Cracking of the NMC secondary particles observed at the moderate to high charging rates (1–3C) indicates that it is not the main mechanism that limits the fast charging capability. XPS and EIS results generally show increased surface film thickness and impedance, respectively, towards the edge of the jellyroll, showing the spatially inhomogeneous ageing that occurs during cycling. A significant discrepancy in the active material losses between that calculated from the cycled cells and from the harvested electrodes show the benefit of the cell voltage fitting technique in capturing the consequences of ageing mechanisms that are overlooked by sample bias or material disturbances during post-mortem analysis. Similarly, the high impedance observed in the cell cycled at 4C caused by the gas generation which induces ionic transport restriction between electrodes in the jellyroll could not be captured by the impedance measurements of the harvest electrodes. Hence, post-mortem analyses and non-destructive online diagnostics techniques should be used as complementary techniques for better understanding of lithium-ion battery ageing.

Acknowledgments

within the Batterifond project *Fast-Charging of Large Energy-optimized Li-ion Cells for Electrified Drivelines (Grant number: P40501-1)* and the Energy Efficient Vehicles program project *Electrochemical study of durability aspects in large vehicle batteries (Grant number: 30770-1)*. The study also had support from the Swedish Electromobility Centre and the governmental initiative Stand-Up for Energy. Dr Jens Groot (AB Volvo) is acknowledged for the helpful discussions. Thanks also to Dr Andrzej Nowak and Maria Varini for some electrochemical measurements. Dr Mario Wachtler and Chao Xu are acknowledged for their help with XPS measurements.

Appendix A. Supplementary data

Supplementary data to this article can be found online at https://doi.org/10.1016/j.jpowsour.2019.02.095.

References

[1] A. Bastian, M. Börjesson, Travel Behav. Soc. 13 (2018) 71–87.
[2] R. Buehler, J. Pucher, R. Gerike, T. Götschi, Transport Rev. 37 (2017) 4–28.
[3] O. O, A. Grauers, P. S, 29th International Electric Vehicle Symposium 2016 (EVS29), 2016, p. 604.
[4] P.D. Prezas, L. Somerville, P. Jennings, A. McGordon, J.K. Basco, T. Duong, I. Bloom, SAE International, 2016.
[5] X. Yang, T. Miller, SAE International, 2017.
[6] M. Shirk, J. Wishart, SAE International, 2015.
[7] T.R. Tanim, M.G. Shirk, R.L. Bewley, E.J. Dufek, B.Y. Liaw, J. Power Sources 381 (2018) 56–65.
[8] K.G. Gallagher, S.E. Trask, C. Bauer, T. Woehrle, S.F. Lux, M. Tschech, P. Lamp, B.J. Polzin, S. Ha, B. Long, Q. Wu, W. Lu, D.W. Dees, A.N. Jansen, J. Electrochem. Soc. 163 (2016) A138–A149.
[9] H. Zheng, J. Li, X. Song, G. Liu, V.S. Battaglia, Electrochim. Acta 71 (2012) 258–265.
[10] J. Vetter, P. Novák, M.R. Wagner, C. Veit, K.C. Möller, J.O. Besenhard, M. Winter, M. Wohlfahrt-Mehrens, C. Vogler, A. Hammouche, J. Power Sources 147 (2005) 269–281.
[11] P. Arora, M. Doyle, R.E. White, J. Electrochem. Soc. 146 (1999) 3543–3553.
[12] N. Ogihara, Y. Itou, T. Sasaki, Y. Takeuchi, J. Phys. Chem. C 119 (2015) 4612–4619.
[13] T. Waldmann, M. Wilka, M. Kasper, M. Fleischhammer, M. Wohlfahrt-Mehrens, J. Power Sources 262 (2014) 129–135.
[14] F. Leng, C.M. Tan, M. Pecht, Sci. Rep. 5 (2015) 12967.
[15] K. Zhao, M. Pharr, J.J. Vlassak, Z. Suo, J. Appl. Phys. 108 (2010) 073517.
[16] S. Brunauer, P.H. Emmett, E. Teller, J. Am. Chem. Soc. 60 (1938) 309–319.
[17] M. Hervieu, C. Michel, B. Domenges, Y. Laligant, A. Lebail, G. Ferey, B. Raveau, Mod. Phys. Lett. B 02 (1988) 491–500.
[18] J.H. Scofield, J. Electron. Spectrosc. Relat. Phenom. 8 (1976) 129–137.
[19] A.S. Mussa, M. Klett, M. Behm, G. Lindbergh, R.W. Lindström, J. Energy Storage 13 (2017) 325–333.
[20] Q. Zhang, R.E. White, J. Power Sources 179 (2008) 793–798.
[21] T.C. Bach, S.F. Schuster, E. Fleder, J. Müller, M.J. Brand, H. Lorrmann, A. Jossen, G. Sextl, J. Energy Storage 5 (2016) 212–223.
[22] H. Lundgren, P. Svens, H. Ekström, C. Tengstedt, J. Lindström, M. Behm, G. Lindbergh, J. Electrochem. Soc. 163 (2016) A309–A317.
[23] C. Uhlmann, J. Illig, M. Ender, R. Schuster, E. Ivers-Tiffée, J. Power Sources 279 (2015) 428–438.
[24] M.J. Lacey, A. Yalamanchili, J. Maibach, C. Tengstedt, K. Edstrom, D. Brandell, RSC Adv. 6 (2016) 3632–3641.
[25] S. Leroy, F. Blanchard, R. Dedryvère, H. Martinez, B. Carré, D. Lemordant, D. Gonbeau, Surf. Interfac. Anal. 37 (2005) 773–781.
[26] A.S. Mussa, G. Lindbergh, M. Klett, P. Gudmundson, P. Svens, R.W. Lindström, J. Energy Storage 20 (2018) 213–217.
[27] A. Devie, M. Dubarry, H.-P. Wu, T.-H. Wu, B.Y. Liaw, J. Electrochem. Soc. 163 (2016) A2611–A2617.
[28] D. Aurbach, J. Power Sources 89 (2000) 206–218.
[29] M. Takeno, T. Fukutsuka, K. Miyazaki, T. Abe, J. Electrochem. Soc. 164 (2017) A3862–A3867.
[30] D. Aurbach, M.D. Levi, E. Levi, H. Teller, B. Markovsky, G. Salitra, U. Heider, L. Heider, J. Electrochem. Soc. 145 (1998) 3024–3034.
[31] J.-M. Atebamba, J. Moskon, S. Pejovnik, M. Gaberscek, J. Electrochem. Soc. 157 (2010) A1218–A1228.
[32] A.S. Mussa, M. Klett, G. Lindbergh, R.W. Lindström, J. Power Sources 385 (2018) 18–26.
[33] B. Streipert, P. Janßen, X. Cao, J. Kasnatscheew, R. Wagner, I. Cekic-Laskovic, M. Winter, T. Placke, J. Electrochem. Soc. 164 (2017) A168–A172.
[34] M. Metzger, B. Strehle, S. Solchenbach, H.A. Gasteiger, J. Electrochem. Soc. 163 (2016) A798–A809.
[35] B. Michalak, B.B. Berkes, H. Sommer, T. Brezesinski, J. Janek, J. Phys. Chem. C 121 (2017) 211–216.
[36] S.F. Schuster, T. Bach, E. Fleder, J. Müller, M. Brand, G. Sextl, A. Jossen, J. Energy Storage 1 (2015) 44–53.
[37] L. Nurhadi, S. Borén, H. Ny, Transport. Res. Procedia 3 (2014) 818–827.